

Photoexcited carriers and surface recombination velocity in InN epilayers: A Raman scattering study

Ramon Cuscó, Jordi Ibáñez, Esther Alarcón-Lladó, and Luis Artús

Institut Jaume Almera, Consell Superior d'Investigacions Científiques (CSIC), Lluís Solé i Sabarís s.n., 08028 Barcelona, Spain

Tomohiro Yamaguchi and Yasushi Nanishi

Faculty of Science and Engineering, Ritsumeikan University, 1-1-1 Noji-Higashi, Kusatsu, Shiga 525-8577, Japan

(Received 22 July 2009; published 27 October 2009)

The effect of photoexcited electron-hole pairs on the LO-phonon-plasmon coupled modes has been observed in InN layers by means of micro-Raman experiments performed at different excitation laser powers. The L^- Raman peak displays an upward shift of about 10 cm^{-1} over the range of increasing excitation powers studied. The L^- behavior is well accounted for by a dielectric line-shape model based on the Lindhard-Mermin dielectric function. The photoexcited carrier density has been extracted from line-shape fits to the Raman spectra and a linear increase in the photoexcited carrier density with incident power is found. A simple diffusion model is used to estimate the surface recombination velocity in the layers, which is found to be in the $4.6\text{--}4.9 \times 10^4\text{ cm s}^{-1}$ range for the bare InN surface.

DOI: [10.1103/PhysRevB.80.155204](https://doi.org/10.1103/PhysRevB.80.155204)

PACS number(s): 78.30.Fs, 63.20.kk

I. INTRODUCTION

Over the last few years, InN has attracted much attention because of its unique properties. A great deal of effort has been devoted to improve the crystal quality of the layers and this has led to the revision of the accepted band-gap energy value^{1,2} and to the demonstration of an extreme electron accumulation at the InN surfaces.³ Despite the remarkable improvement in the epitaxial growth of InN films achieved in recent years, InN layers still contain a high density of dislocations, which affect their optical and electrical properties. N vacancies associated with threading dislocations may partly be the source of the n -type conductivity generally observed in nominally undoped InN layers.⁴ The presence of a surface accumulation layer with a high electron density complicates the analysis of Hall effect measurements to determine the “bulk” electron density in the InN films. The accumulation layer also precludes the formation of a Schottky barrier at the metal/InN interface⁵ and, therefore, the modulation of the background electron density by electrostatic gating is not straightforward.⁶

Raman scattering by LO-phonon-plasmon coupled modes (LOPCMs) can provide an alternative probe into the free-electron density present in InN layers.⁷ Some early works^{8,9} on Raman scattering by LOPCMs in InN invoked impurity-induced wave-vector nonconserving mechanisms to assign a Raman peak close to the $A_1(\text{LO})$ frequency to large-wave-vector LOPCMs. The frequency of such a peak is rather insensitive to the free-electron density⁸ and, therefore, cannot serve as a reliable indication of the free-electron density. However, we have recently shown that Raman scattering by long-wavelength LOPCMs does take place in high-mobility InN layers.⁷ In that work, we reported the distinct observation of the L^- Raman peak in a set of InN layers with different background electron densities N_e^0 . The frequency of the L^- peak was observed to increase by about 40 cm^{-1} as N_e^0 increased from $4 \times 10^{18}\text{ cm}^{-3}$ up to $2 \times 10^{19}\text{ cm}^{-3}$. Such a sensitivity allows the background electron density in the InN

layers to be determined from line-shape fits to the L^- Raman spectra.

While the electron density in the InN layers cannot be controlled by an electrostatic potential applied to a metal gate, it is possible to modulate the free-charge density by optical excitation with above band-gap photons. Provided that the surface recombination velocity (SRV) is not too high, a spatially homogeneous population of electron-hole pairs can be sustained by continuous wave (CW) laser excitation.^{10,11} In this work we use micro-Raman spectroscopy to study the dependence on excitation power of the L^- coupled mode in InN layers under high photon flux density conditions. We observe an upward frequency shift of the L^- mode with increasing excitation power and from Raman line-shape fits we can extract the density of photoexcited electron-hole pairs. Besides the information about the free carrier density in the InN layers, the analysis of the Raman data using a simple diffusion model allows us to estimate the SRV at the InN interfaces.

II. EXPERIMENT

The Raman experiments were carried out on two nominally undoped InN epilayers: A1 and A4 (see Ref. 7 for details). Sample A1 was chosen because its background electron density was relatively low and no L^- coupled-mode peak could be detected in the experiments reported in Ref. 7. For comparison, we also studied the sample with the highest background electron density in the same series (sample A4).

Layer A1 is 550 nm thick and was grown with the repetition of droplet elimination by radical beam irradiation method¹² by plasma-assisted molecular beam epitaxy (PA-MBE) on a GaN/sapphire template at $\sim 450^\circ\text{C}$. Layer A4 is 250 nm thick and was grown by PA-MBE on a nitridated (0001) sapphire substrate at $\sim 450^\circ\text{C}$.

Standard Hall effect measurements yielded a background electron concentration $N_e^0 = 2.3 \times 10^{18}\text{ cm}^{-3}$ and an electron mobility $\mu_e = 1440\text{ cm}^2\text{ V}^{-1}\text{ s}^{-1}$ for sample A1. For sample

A4 we obtained $N_e^0 = 6.9 \times 10^{18} \text{ cm}^{-3}$ and $\mu_e = 900 \text{ cm}^2 \text{ V}^{-1} \text{ s}^{-1}$.

Micro-Raman spectra were recorded at room temperature in $z(x)\bar{z}$ backscattering geometry, where z is parallel to the wurtzite InN c axis, using a Jobin-Yvon T64000 spectrometer equipped with a charge coupled device detector cooled with liquid nitrogen. The excitation wavelength used was the 514.5 nm line of an Ar^+ laser. The incident power was measured on the sample location and it was varied from 1.8 up to 12.0 mW. The laser beam was focused to a $\sim 1 \mu\text{m}$ diameter spot through a $\times 100$ objective.

III. RESULTS AND DISCUSSION

A. Observation of photoexcitation effects in LO-phonon-plasmon coupled modes

Photoexcited electron-hole plasmas generated by optically pumping a semiconductor with above band-gap excitation have been used for a number of years in time-resolved Raman scattering experiments to investigate hot carrier and multicomponent plasma dynamics mainly in GaAs (Refs. 13 and 14) and InP.^{15,16} It was realized that the qualitative differences observed in Raman scattering by photoexcited LOPCMs in GaAs and InP could be traced to the extremely large recombination velocity at the bare GaAs surface.¹⁰ This leads to a highly inhomogeneous plasma in GaAs which obscures the well-known coupling between LO phonons and homogeneous plasmas. In contrast, InP exhibits a SRV more than three orders of magnitude lower,¹⁷ which results in a relatively homogeneous density profile within the skin depth and allows LOPCMs to be observed in time-resolved Raman scattering experiments.^{15,16} By the same token, photoexcitation effects in Raman scattering measurements under CW laser excitation are important in InP (Refs. 11 and 18) whereas they are not observed in GaAs.¹⁸

A general criterion based on the position of the average dangling bond energy relative to the band edges has been proposed to account for the SRV trend in several III-V semiconductors.¹⁹ According to this criterion, the chemical trends in the SRV can be qualitatively predicted using the location of the Fermi-level stabilization energy²⁰ relative to the band edges. As in the case of InP or InAs, the Fermi-level stabilization energy of InN lies close to the conduction-band edge and, therefore, a low SRV is to be expected. In addition, the strong electrostatic fields in the surface accumulation layer may also contribute to lower the SRV by confining minority carriers in the bulk.²¹ InN is therefore expected to be a good candidate to observe photoexcitation effects in Raman scattering experiments.

No apparent differences were observed in the LOPCM spectra of InN layers reported in Ref. 7 when the excitation power was varied. This indicates that the photoexcitation level achieved by CW pumping with a laser beam focused using conventional macrocamera optics is well below the background electron density in the layers. To investigate CW photoexcitation effects in InN layers we have carried out micro-Raman experiments in which the photon flux density is more than three orders of magnitude higher. Figure 1 displays the Raman spectra of the L^- modes for samples A1 and

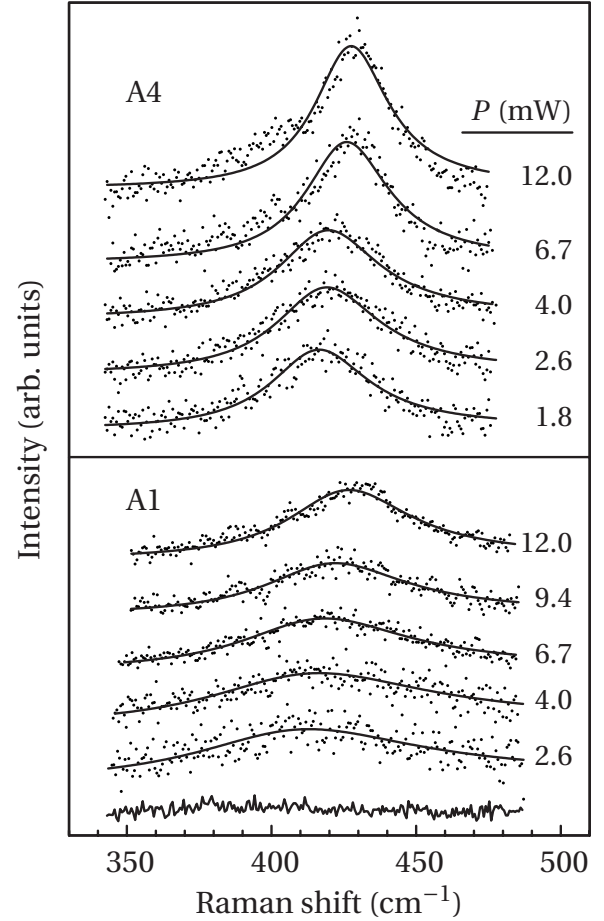


FIG. 1. Room temperature $z(x)\bar{z}$ Raman scattering spectra (dots) of the L^- modes for samples A1 (lower panel) and A4 (upper panel) obtained at different excitation laser powers in micro-Raman configuration with $\sim 1 \mu\text{m}$ spot size. For comparison purposes, the intensity of each spectrum has been normalized to that of the E_2^{high} mode. The solid lines are calculated L^- line shapes obtained by fitting the model described in Sec. III B to the Raman spectra. The continuous trace at the bottom of the lower panel corresponds to the spectrum taken with $P = 150 \text{ mW}$ in macrocamera configuration.

A4 recorded at different excitation powers. To facilitate the comparison between L^- Raman peaks recorded at different excitation powers, the intensities of the spectra have been normalized to that of the E_2^{high} mode. A Lorentzian line shape corresponding to the E_2^{high} mode which appears in the spectra at around 490 cm^{-1} as well as a weak background signal which is probably related to surface roughness have been subtracted in all of the spectra. The L^- spectra obtained at increasing excitation power have been vertically shifted for clarity. Given the low background electron density of sample A1, the L^- peak could not be unambiguously detected in the spectrum taken in macrocamera configuration (bottom trace in Fig. 1). In contrast, the spectrum taken with the micro-Raman setup at the lowest power (2.6 mW) already shows a weak band at $\approx 415 \text{ cm}^{-1}$. With increasing excitation power, the signal-to-noise ratio improves and the L^- peak becomes more definite. As the power is increased, the L^- peak clearly increases in intensity and shifts to higher frequencies

($\approx 430 \text{ cm}^{-1}$ for 12.0 mW excitation power). Thus, although the background electron density in sample A1 was too low for the observation of the L^- peak by means of conventional Raman measurements,⁷ the higher level of optical pumping achieved in the micro-Raman setup has revealed the presence of the L^- mode in this sample. On the other hand, the background electron density in sample A4 was high enough to allow the unambiguous observation of the L^- mode in conventional macrocamera measurements.⁷ In the case of micro-Raman measurements, a distinct L^- peak is already observed with the lowest excitation power (1.8 mW). In this sample, the L^- peak also shows an intensity enhancement and an upward frequency shift as the excitation power is increased up to 12.0 mW, which reflects the additional contribution of the photoexcited carriers to the plasma frequency. Thus, optical pumping at high excitation levels injects a density of photoexcited carriers which is high enough to allow the L^- mode to emerge in samples with low N_e^0 and to shift to higher frequencies in layers with higher N_e^0 . We note that the width of the L^- peak in the spectra of sample A1 is larger than in the spectra of sample A4 even for similar electron densities. Since sample A1 has a low background electron density and no unambiguous L^- peak could be detected under low power excitation conditions, the photoexcited carriers represent the main contribution to the L^- coupled mode observed in the micro-Raman measurements on sample A1. In contrast, sample A4 has a substantial background electron density and photoexcited carriers represent only a fraction of the total free carrier density. Then, the larger width of the L^- peak in the spectra of sample A1 probably reflects carrier-density variations across the photoexcited density profile probed by the Raman measurements, which, as discussed in more detail in Sec. III C, arise from the diffusion of the photoexcited carriers. In the next section we shall discuss the effect of the photoexcited carriers on the LOPCMs and we shall present a line-shape model that will allow us to estimate the density of photoexcited carriers from the L^- Raman spectra.

B. L^- line-shape model and photoexcited carrier-density determination

The Raman line shape of the LOPCMs can be accurately modeled by the standard dielectric theory in the formalism of Hon and Faust.²² Details on the application of this model to the calculation of LOPCM Raman line shapes in n -type InN can be found in Ref. 7. In the case of optically pumped InN layers we have to deal with a two-component plasma that consists of background and photoexcited electrons on the one hand and photoexcited holes on the other. A number of simplifying assumptions will be made to render the complex problem of multicomponent plasmas tractable under the present framework. First, we assume that electrons and holes give additive contributions to the electronic susceptibility.²³ Second, since recent InN band-structure calculations²⁴ suggest a rather flat heavy hole (HH) band with a revised effective mass value of $m_{\text{HH}}^{\parallel} = 2.566m_e$, we assume that most of the photoexcited holes are in the HH band. A rough estimation indicates that the highly anisotropic light hole (LH) band starts to be populated when $N_{\text{HH}} \sim 2 \times 10^{18} \text{ cm}^{-3}$. For N_{HH}

$\sim 5 \times 10^{18} \text{ cm}^{-3}$, which, as we shall see below, is of the order of the highest photoexcited densities that we find in our experiments, the LH population is still one order of magnitude smaller. Thus, we neglect interband hole transitions as well as the LH contribution to the electronic susceptibility. Further, we consider a parabolic isotropic approximation for the HH band dispersion. Then, we use the Lindhard-Mermin model [Eqs. (3) and (4) of Ref. 7] to evaluate the electronic susceptibility of an electron plasma of density $N_e^0 + N_{\text{ph}}$ and a HH plasma of density N_{ph} , where N_{ph} is the density of photoexcited electron-hole pairs. To reduce the number of fitting parameters, a fixed damping value for the HH plasma estimated from typical hole mobility values ($\mu_h \sim 25 \text{ cm}^2 \text{ V}^{-1} \text{ s}^{-1}$) reported in the literature^{25,26} was used in the calculations.

Given the high power densities involved in the micro-Raman measurements, local heating effects must be taken into account in the analysis of the Raman spectra recorded at different incident powers. Temperature variations due to local heating effects were evaluated from the frequency shift of the E_2^{high} mode using the curve reported in Ref. 27. In our Raman spectra, the E_2^{high} peak displays a typical downward frequency shift of $\sim 1.4 \text{ cm}^{-1}$ between the lowest (1.8 mW) and the highest excitation power (12 mW) used, from which we estimate a temperature increase of $\sim 60 \text{ }^\circ\text{C}$. The corresponding temperature corrections to the A_1 phonon frequencies, which enter as parameters of the line-shape model, were effected using the temperature-dependence curve given in Ref. 27. A correction to account for the different strain state of layers A1 and A4 (see Ref. 7) was also included. For that purpose, following Ref. 7, biaxial strain in the layers was determined from the E_2^{high} frequency obtained in the macrocamera experiments and then the strain-induced shift of the A_1 modes was evaluated using the deformation potentials reported in Ref. 28. $A_1(\text{TO})$ values corrected for temperature and strain ranged from 451.6 to 453.6 cm^{-1} for sample A1 and from 448.5 to 449.8 cm^{-1} for sample A4. For sample A4, we estimate that a variation of the A_1 frequencies by 1 cm^{-1} , typical of temperature corrections, yields an error of $\sim 5\%$ in the carrier density determination, while the error for a deviation of 3 cm^{-1} , typical of strain corrections, is $\sim 15\%$.

The photoexcited carrier density N_{ph} was extracted from line-shape model fits to the Raman spectra. Since the LOPCMs depend on both the background electron density and on the photoexcited carrier density, to reduce the number of fitting parameters the following procedure was adopted. An initial estimate of the total free-electron density $N_e = N_e^0 + N_{\text{ph}}$ was obtained by neglecting the HH contribution and using N_e and the phenomenological electronic damping constant Γ_e as free parameters in the fit. As starting point, we took as N_e^0 the value obtained by Hall measurements. In subsequent steps, we included the HH contribution with a photoexcited carrier density given by the difference between the fitted value N_e and the input background density N_e^0 . The fitting process was iterated until self-consistency in the N_e values was reached. Using the N_e values obtained for the different excitation powers P , an extrapolated value of N_e for $P=0$ was derived and subsequently used as a new N_e^0 value in the fits. The process was iterated again until self-consistent

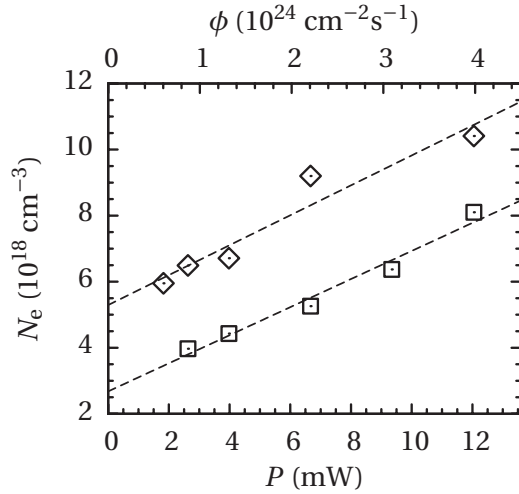


FIG. 2. Free-electron density in the InN layers as a function of the incident power for samples A1 (squares) and A4 (diamonds). The top scale gives the corresponding photon flux density considering a spot size of $1 \mu\text{m}\varnothing$. The dashed lines are linear fits to the data. The intercepts with the N_e axis at $P=0$ give the background electron density in the layers.

values of N_e for $P \rightarrow 0$ were obtained. In this way, we obtain a determination of the background electron density which is consistent with the set of Raman spectra being analyzed. For sample A1 we find $N_e(P \rightarrow 0) = 2.7 \times 10^{18} \text{ cm}^{-3}$, which is not far from the electron density determined by Hall measurements. We note that by using this procedure, the background electron density of the A1 layer could be determined from Raman scattering measurements despite the fact that the free-electron density was too low to unambiguously detect the L^- peak in the low power excitation measurements carried out in macrocamera configuration. For sample A4 we find $N_e(P \rightarrow 0) = 5.3 \times 10^{18} \text{ cm}^{-3}$. Taking into account the different experimental conditions of temperature and probed scattering volume, this value is in reasonable agreement with the electron density determined by line-shape fits to 80 K Raman spectra previously reported in Ref. 7, although it is sizably lower than the Hall effect determination. The larger discrepancy between Hall and micro-Raman N_e determinations found in sample A4 may be attributed to the effects of the surface accumulation layer on the Hall measurements, which are more pronounced in the case of the thinner A4 epilayer.

The fitted theoretical L^- line shapes are displayed in Fig. 1 as solid lines superimposed to the corresponding Raman spectra (dots). The model reproduces nicely the observed behavior of the L^- Raman peak. The free-electron density extracted from the line-shape fits as a function of the incident power, or equivalently, as a function of the photon flux density ϕ , are plotted in Fig. 2. A linear dependence of the free-electron density with the excitation power density is found. The intercept with the N_e axis at $\phi=0$ gives the background electron density in the layers arising from the presence of threading dislocations and unintentional impurities. Although the background electron density is quite different in samples A1 and A4, they exhibit a similar rate of N_e increase with photon flux density. The density of photoexcited carriers under CW excitation is expected to be proportional

TABLE I. Input parameters for the diffusion model used to analyze the photoexcitation effects in the InN layers.

Symbol	Description	Value	Ref.
D	Ambipolar diffusion coefficient	$2.01 \text{ cm}^2 \text{ s}^{-1}$	25
τ	Recombination time	$5.4 \times 10^{-9} \text{ s}$	25
α	Absorption coefficient	$1.385 \times 10^5 \text{ cm}^{-1}$	30
R	Reflectivity coefficient	0.2	31
w_o	Focused beam waist	$5.0 \times 10^{-5} \text{ cm}$	^a

^aNominal laser spot radius with a $\times 100$ objective according to system specifications.

to the incident power density and the steady-state population of photoexcited carriers is ultimately determined by the recombination rate of the electron-hole pairs at native defect levels in the bulk and on the surface of the semiconductor. In thin films and devices with small active thickness, surface recombination plays a major role in limiting the quantum efficiency of radiative processes.²⁹ To extract information about the SRV in the studied InN layers, in the next section we analyze our photoexcited plasma results in the light of a simple steady-state diffusion-recombination model.

C. Photoexcited density and surface recombination velocity

Since the surface accumulation layer is extremely narrow ($\sim 2 \text{ nm}$), the electrons in this layer cannot support longitudinal excitations along z and, therefore, the observed L^- peaks correspond to the bulk LOPCMs in the InN layers.⁷ Thus, the main effect of the presence of the accumulation layer on the photoexcited carrier behavior studied in this work lies in its influence on the SRV values, which enter as parameters in the diffusion-recombination model. Then, aside from its effect on SRV values, the presence of an accumulation layer shall be ignored in the following analysis of the Raman spectra of photoexcited carriers.

Owing to the mass difference between electrons and holes, electric fields develop between photoexcited electrons and holes that result in a coupled diffusive motion. The ambipolar diffusion coefficient D has been determined in InN layers by means of time-resolved transient spectroscopy.²⁵ Assuming a constant recombination rate τ^{-1} in the bulk, the steady-state distribution of photoexcited carriers along z is governed by the one-dimensional (1D) continuity equation

$$D \frac{d^2 N_{\text{ph}}}{dz^2} + G(z) = \frac{N_{\text{ph}}}{\tau}. \quad (1)$$

Here, $G(z) = \alpha(1-R)\phi e^{-\alpha z}$ is the generation term, where α is the absorption coefficient, R is the reflection coefficient, and ϕ is the incident photon flux density. The general solution of Eq. (1) is

$$N_{\text{ph}}(z) = \frac{G(0)}{1 - (l\alpha)^2} (e^{-\alpha z} + A e^{-z/l} + B e^{z/l}), \quad (2)$$

where $l = \sqrt{D\tau}$ is the ambipolar diffusion length. Numerical values for the model parameters are listed in Table I. The constants A and B depend on the SRV values at the surface

and at the substrate interfaces, S_0 and S_d respectively. A and B can be obtained as algebraic expressions in S_0 and S_d from the carrier loss rate at the interfaces $z=0$ and $z=d$,

$$\left. \begin{aligned} N_{\text{ph}}(0)S_0 &= D \left(\frac{dN_{\text{ph}}}{dz} \right)_{z=0} \\ N_{\text{ph}}(d)S_d &= -D \left(\frac{dN_{\text{ph}}}{dz} \right)_{z=d} \end{aligned} \right\}. \quad (3)$$

According to Eq. (2), the photoexcited carrier density is proportional to the photon flux density as we have found in our Raman experiments carried out under different excitation powers. Then, Eq. (2) can be used to estimate the SRV from the slope of the plots displayed in Fig. 2.

However, the simple one-dimensional model we have just discussed grossly overestimates the photoexcited carrier density because it does not take into account the lateral out-diffusion of the electron-hole pairs away from the laser beam axis. This effect is usually neglected in the time-resolved analysis of photoinjected plasmas^{10,15,16} and in steady-state plasmas under CW excitation in which the laser is focused to a spot size much larger than the diffusion length.¹¹ However, in the case of micro-Raman experiments the beam waist w_0 of the focused laser beam is $w_0 \lesssim l$, and therefore carrier loss due to lateral out-diffusion is expected to be substantial. To account for this effect, we solve the steady-state diffusion equation in the plane perpendicular to the laser beam considering the Gaussian profile of the laser beam. The radial part of the diffusion equation is

$$D \left(\frac{\partial^2 N_{\text{ph}}}{\partial \rho^2} + \frac{1}{\rho} \frac{\partial N_{\text{ph}}}{\partial \rho} \right) + \alpha(1-R)\phi e^{-2(\rho/w_0)^2} - \frac{N_{\text{ph}}}{\tau} = 0. \quad (4)$$

A convenient scaling of Eq. (4) is obtained by expressing the carrier density in units of the peak carrier density in absence of diffusion, $N_0 = \alpha(1-R)\phi\tau$, and the radial distance in units of the laser beam waist, w_0 . We make a Taylor's expansion around the regular singular point $\rho=0$ of a solution of Eq. (4) that satisfies the boundary condition $(\partial N_{\text{ph}}/\partial \rho)_{\rho=0}=0$ and we propagate numerically this solution to larger ρ . The zeroth-order coefficient of the Taylor expansion is then adjusted to yield a carrier-density distribution that vanishes at large ρ . The radial distribution profile of the photoexcited carriers obtained for the parameters listed in Table I is shown in Fig. 3.

To assess the effect of lateral diffusion, we compare this profile with the one that would result in absence of carrier diffusion [$D=0$ in Eq. (4)]. The latter is shown, scaled down by a factor of 10, as a dashed line in Fig. 3. We can see that a large fraction of the photogenerated carriers diffuse to a region outside the Gaussian profile of the laser beam. As a consequence, we estimate that the carrier density probed by the micro-Raman experiment is reduced by a multiplicative factor of ≈ 0.089 relative to the case in which radial diffusion is neglected, as obtained from the ratio between the corresponding peak densities at the beam axis. Thus, we apply this correction factor to the density distribution derived from Eq. (1) to compare the 1D-diffusion model with the experimental determination of the photoexcited carrier density from micro-Raman experiments. Further, to account for the finite

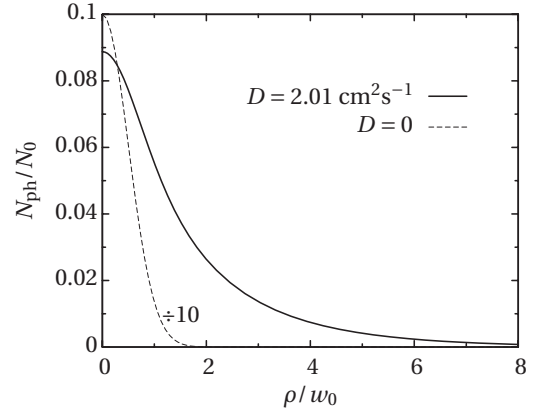


FIG. 3. Radial distribution around the laser beam axis of the photoexcited carrier density taking into account the ambipolar diffusion of the electron-hole pairs. The dashed line depicts the density profile that would result in absence of carrier diffusion. Note that carrier density is given in units of the peak density in absence of diffusion, N_0 , and the radial distance in units of the laser beam waist, w_0 .

Raman probing depth we consider an average of the photoexcited carrier profile weighted by the optical attenuation factor

$$\langle N_{\text{ph}} \rangle = \frac{\int_0^d N_{\text{ph}}(z) e^{-2\alpha z} dz}{\int_0^d e^{-2\alpha z} dz}. \quad (5)$$

By equating $\langle N_{\text{ph}} \rangle$ with the photoexcited carrier-density values derived from the micro-Raman measurements (linear fits in Fig. 2), we can determine the SRV in the layers studied. Owing to the large number of dangling bonds at exposed surfaces, the SRV at the semiconductor/air interface is generally higher than that at heterointerfaces, where recombination occurs mainly at misfit dislocations.²⁹ We may safely assume that the SRV at the exposed InN surface, S_0 , must be the same for both layers, and that S_0 is higher than the SRV at the InN/substrate interface. Then, to determine the SRV values, we evaluate S_0 for both layers as a function of the S_0/S_d ratio. The results are shown in Fig. 4, where we can see that the curves corresponding to samples A1 and A4 cross at $S_0/S_d \approx 21.5$. For this particular SRV ratio, the SRV at the InN/substrate surface would also be the same for both samples. Given that sample A1 displays a lower background electron density than sample A4, it is likely that the GaN/InN interface of sample A1 is of superior quality than the nitrated sapphire/InN interface of sample A4 and, therefore, S_d may be expected to be somewhat higher for the latter. This is consistent with Fig. 4 if we consider SRV ratios $S_0/S_d \gtrsim 21.5$. Then, for a given SRV at the InN/air interface S_0 , one can find SRV values at the InN/substrate interface $S_d^{(A1)}$ and $S_d^{(A4)}$ such that $S_d^{(A1)} \lesssim S_d^{(A4)}$. Taking into account the asymptotic behavior of the curve A1 at large S_0/S_d , we may estimate the SRV at the InN/air interface to be in the $4.6\text{--}4.9 \times 10^4 \text{ cm s}^{-1}$ range. This value is comparable to SRV estimates in GaN for which an upper limit of $3 \times 10^4 \text{ cm s}^{-1}$ was determined from absolute photoluminescence quantum efficiency measurements.³²

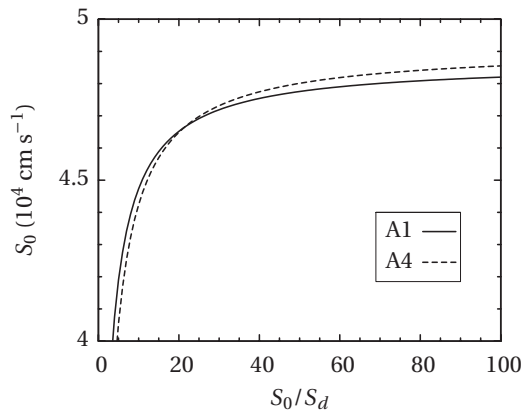


FIG. 4. Surface recombination velocity at the InN/air interface as a function of the ratio between surface recombination velocities at the sample surface and at the substrate interface for samples A1 and A4.

In contrast with GaAs, for which SRV values as high as $5 \times 10^8 \text{ cm s}^{-1}$ have been proposed,¹⁰ the SRV in InN layers is low enough to produce a photoexcited plasma with a charge density profile that does not vary substantially over the Raman probing depth. This is illustrated in Fig. 5, where we have plotted the depth profile of the photoexcited charge for samples A1 and A4 calculated with the S_0 and S_d values determined above. The small variation in carrier density within the optical skin depth allows coupled-mode peaks to be observed in Raman scattering measurements. The smaller SRV in InN as compared to GaAs is consistent with the Fermi-level stabilization energy criterion.¹⁹ The SRV in InN is, however, greater than in InP, for which it was estimated to be $S \sim 10^2 \text{ cm s}^{-1}$.³³ Indeed, photoexcitation effects in Raman scattering by LOPCMs were reported for semiconducting InP at excitation power densities more than three orders of magnitude lower than those used in the present work.¹¹

IV. CONCLUSIONS

We have observed photoexcitation effects in the Raman scattering spectra of LOPCMs obtained from InN layers under high levels of CW laser excitation. Micro-Raman experiments have revealed the presence of the L^- mode in an InN layer with low N_e^0 for which no L^- peak could be detected in conventional macrocamera Raman measurements. The observed shift of the L^- Raman peak, which indicates a significant steady-state population of electron-hole pairs, is well accounted for by the dielectric LOPCM line-shape model. The photoexcited carrier density is found to increase linearly with the excitation power density. The responsiveness of the

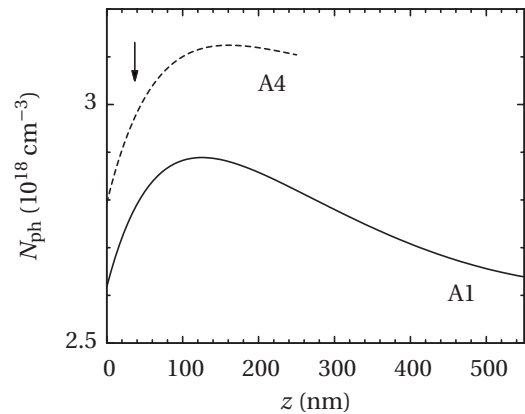


FIG. 5. Depth profile of the photoexcited carrier density in layers A1 and A4 as calculated from the 1D diffusion equation for a photon flux density of $2.2 \times 10^{24} \text{ cm}^{-2} \text{ s}^{-1}$. The arrow indicates the Raman probing depth $1/(2\alpha)$. Note that the layer thickness for sample A4 is 250 nm.

L^- peak to the modulation of the free carrier density by means of optical pumping confirms our previous assignment of this peak to a long-wavelength LOPCM and corroborates the fact that wave-vector conserving scattering by LOPCMs takes place in InN. The sensitivity of the L^- mode allows us to extract the photoexcited carrier density from line-shape fits to the Raman spectra. By extrapolating the photoexcited carrier density to zero power excitation we have been able to determine from the Raman experiments the background electron density of an InN layer whose free-electron density was too low to unambiguously detect the L^- peak in conventional Raman measurements performed at lower excitation power density.

From the analysis of these data using a simple diffusion model, an estimate of the SRV in these InN layers can be obtained. The relatively low SRV values found give rise to a homogeneous profile of the photoexcited density within the Raman probing depth, which allows LOPCM Raman peaks to be observed even in samples with low background electron density on account of photoexcitation effects. SRV in the InN layers studied is, however, substantially higher than in the case of InP and, therefore, photoexcitation effects in InN are revealed only under the high power-density conditions achieved in micro-Raman experiments.

ACKNOWLEDGMENTS

This work was supported by the Spanish Ministry of Science and Innovation under Contract No. MAT2007-63617.

¹J. Wu, W. Walukiewicz, K. M. Yu, J. W. Ager III, E. E. Haller, H. Lu, and W. J. Schaff, *Appl. Phys. Lett.* **80**, 4741 (2002).

²V. Y. Davydov, A. A. Klochikhin, V. V. Emtsev, D. A. Kurdyukov, S. V. Ivanov, V. A. Vekshin, F. Bechstedt, J. Furth-

müller, J. Aderhold, J. Graul, A. V. Mudryi, H. Harima, A. Hashimoto, A. Yamamoto, and E. E. Haller, *Phys. Status Solidi B* **234**, 787 (2002).

³I. Mahboob, T. D. Veal, C. F. McConville, H. Lu, and W. J.

- Schaff, Phys. Rev. Lett. **92**, 036804 (2004).
- ⁴M. C. Lee, H. C. Lin, Y. C. Pan, C. K. Shu, J. Ou, W. H. Chen, and W. K. Chen, Appl. Phys. Lett. **73**, 2606 (1998).
- ⁵H. Lu, W. J. Schaff, L. F. Eastman, and C. E. Stutz, Appl. Phys. Lett. **82**, 1736 (2003).
- ⁶G. F. Brown, J. W. Ager III, W. Walukiewicz, W. J. Schaff, and J. Wu, Appl. Phys. Lett. **93**, 262105 (2008).
- ⁷R. Cuscó, J. Ibáñez, E. Alarcon-Lladó, L. Artús, T. Yamaguchi, and Y. Nanishi, Phys. Rev. B **79**, 155210 (2009).
- ⁸J. W. Pomeroy, M. Kuball, C. H. Swartz, T. H. Myers, H. Lu, and W. J. Schaff, Phys. Rev. B **75**, 035205 (2007).
- ⁹J. S. Thakur, D. Haddad, V. M. Naik, R. Naik, G. W. Auner, H. Lu, and W. J. Schaff, Phys. Rev. B **71**, 115203 (2005).
- ¹⁰J. F. Young, K. Wan, A. J. SpringThorpe, and P. Mandeville, Phys. Rev. B **36**, 1316 (1987).
- ¹¹R. Cuscó, J. Ibáñez, and L. Artús, Phys. Rev. B **57**, 12197 (1998).
- ¹²T. Yamaguchi and Y. Nanishi, Appl. Phys. Express **2**, 051001 (2009).
- ¹³J. A. Kash, J. C. Tsang, and J. M. Hvam, Phys. Rev. Lett. **54**, 2151 (1985).
- ¹⁴A. Pinczuk, J. Shah, and P. A. Wolff, Phys. Rev. Lett. **47**, 1487 (1981).
- ¹⁵J. F. Young and K. Wan, Phys. Rev. B **35**, 2544 (1987).
- ¹⁶K. T. Tsen, G. Halama, O. F. Sankey, S. C. Y. Tsen, and H. Morkoc, Phys. Rev. B **40**, 8103 (1989).
- ¹⁷D. D. Nolte, Solid-State Electron. **33**, 295 (1990).
- ¹⁸T. Nakamura and T. Katoda, J. Appl. Phys. **55**, 3064 (1984).
- ¹⁹J. M. Langer and W. Walukiewicz, Mater. Sci. Forum **196-201**, 1389 (1995).
- ²⁰J. Tersoff, Phys. Rev. Lett. **52**, 465 (1984).
- ²¹J. S. Rimmer, J. M. Langer, M. Missous, J. H. Evans, I. Poole, A. R. Peaker, and K. Singer, Mater. Sci. Eng., B **9**, 375 (1991).
- ²²D. T. Hon and W. L. Faust, Appl. Phys. **1**, 241 (1973).
- ²³*Light Scattering in Solids IV*, Topics in Applied Physics Vol. 54, edited by M. Cardona and G. Güntherodt (Springer-Verlag, Berlin, 1984).
- ²⁴D. Fritsch, H. Schmidt, and M. Grundmann, Phys. Rev. B **69**, 165204 (2004).
- ²⁵F. Chen, A. N. Cartwright, H. Lu, and W. J. Schaff, Appl. Phys. Lett. **87**, 212104 (2005).
- ²⁶X. Wang, S.-B. Che, Y. Ishitani, and A. Yoshikawa, Appl. Phys. Lett. **92**, 132108 (2008).
- ²⁷X. D. Pu, J. D. Chen, W. Z. Shen, H. Ogawa, and Q. X. Guo, J. Appl. Phys. **98**, 033527 (2005).
- ²⁸X. Wang, S. B. Che, Y. Ishitani, and A. Yoshikawa, Appl. Phys. Lett. **89**, 171907 (2006).
- ²⁹D. E. Aspnes, Surf. Sci. **132**, 406 (1983).
- ³⁰A. Kasic, E. Valcheva, B. Monemar, H. Lu, and W. J. Schaff, Phys. Rev. B **70**, 115217 (2004).
- ³¹V. A. Tyagai, A. M. Estigneev, A. N. Krasiko, A. F. Andreeva, and V. Y. Malakov, Sov. Phys. Semicond. **11**, 1257 (1977).
- ³²M. Boroditsky, I. Gontijo, M. Jackson, R. Vrijen, E. Yablonovith, T. Krauss, C.-C. Cheng, A. Scherer, R. Bhat, and M. Krames, J. Appl. Phys. **87**, 3497 (2000).
- ³³V. Diadiuk, S. H. Groves, C. A. Armiento, and C. E. Hurwitz, Appl. Phys. Lett. **42**, 892 (1983).